Dovepress
Taylor & Francis Group

ORIGINAL RESEARCH

Targeted Nanoclusters for Intratracheal Delivery in Intraoperative Imaging of Lung Adenocarcinoma

Lu Tang[1], Ning Li[2], Zhe Yang[3], Yangliu Lin[4], Ge Gao[5], Quan Lin[4], Yue Wang[6]

[1]Department of Breast Surgery, China-Japan Union Hospital of Jilin University, Changchun, Jilin, People's Republic of China; [2]Department of Respiratory Medicine, China-Japan Union Hospital of Jilin University, Changchun, Jilin, People's Republic of China; [3]Shandong Laboratory of Advanced Materials and Green Manufacturing at Yantai, Yanatai, Shandong, People's Republic of China; [4]State Key Laboratory of Supramolecular Structure and Material, College of Chemistry, Jilin University, Changchun, Jilin, People's Republic of China; [5]Department of Pathology, China-Japan Union Hospital of Jilin University, Changchun, Jilin, People's Republic of China; [6]Department of Thoracic Surgery, China-Japan Union Hospital of Jilin University, Changchun, Jilin, People's Republic of China

Correspondence: Yue Wang, Department of Thoracic Surgery, China-Japan Union Hospital of Jilin University, Changchun, Jilin, People's Republic of China, Tel/Fax +86 431-84995495, Email w_yue@jlu.edu.cn; Quan Lin, State Key Laboratory of Supramolecular Structure and Material, College of Chemistry, Jilin University, Changchun, Jilin, People's Republic of China, Email linquan@jlu.edu.cn

Background: Computed tomography (CT) is widely used all over the world, and the detection rate of early lung adenocarcinoma is increasing. Minimally invasive thoracic surgery (MITS) has emerged as the preferred surgical approach for lung adenocarcinoma, but identifying small lung adenocarcinomas is difficult. Therefore, there is a need for a non-invasive, convenient and efficient way to localize lung adenocarcinomas.

Materials and Methods: A targeted gold nanocluster for intraoperative fluorescence imaging by intratracheal delivery has been designed. Au-GSH-anti Napsin A nanoclusters (NapA-AuNCs) were synthesized, and their physicochemical properties and optical properties were characterized. Target effect, cytotoxicity and fluorescence time curve of NapA-AuNCs, were tested in vivo and in vitro, and intratracheal delivery was also carried.

Results: NapA-AuNCs targeting lung adenocarcinoma with red fluorescence and good mucus penetration were synthesized, which had the targeting property of A549 and lung adenocarcinoma tissue, and also had very low toxicity to normal lung epithelial cells and organs. Intracheal delivery involves faster imaging of lung adenocarcinoma and less accumulation of other organs than intravenous administration.

Conclusion: NapA-AuNCs targeting lung adenocarcinoma were successfully conjugated, and intratracheal delivery is a safe, effective for lung adenocarcinoma intraoperative localization.

Plain Language Summary: Computed tomography (CT) is widely used all over the world, and the detection rate of early lung adenocarcinoma is increasing. But some pulmonary nodules are too small to find when surgically removing them. Therefore, there is a need for a non-invasive, convenient and efficient way to localize lung nodules. We have prepared a nanoparticle (NapA AuNCs) that can make lung adenocarcinoma emit red fluorescence. It can be intratracheal delivered into the lungs through the airway, causing lung adenocarcinoma to emit red fluorescence and remain in the body for a longer period of time. Our experiments on cells and animals have confirmed its effectiveness and low toxicity. Therefore, we believe that this targeted localization method for lung adenocarcinoma has the potential to be applied clinically.

Keywords: lung adenocarcinoma, intraoperative localization, fluorescence imaging, gold nanoparticles, intratracheal delivery, Napsin A

Introduction

Computed tomography (CT) is widely used all over the world, and the detection rate of early lung adenocarcinoma is increasing. When a lung nodule that is >8 mm in diameter has a high malignant probability, a non-surgical biopsy is always selected as a definitive diagnostic procedure.[1] Minimally invasive thoracic surgery (MITS) including video-assisted thoracoscopic surgery (VATS) and robotic-assisted thoracic surgery (RATS) has emerged as the preferred

Graphical Abstract
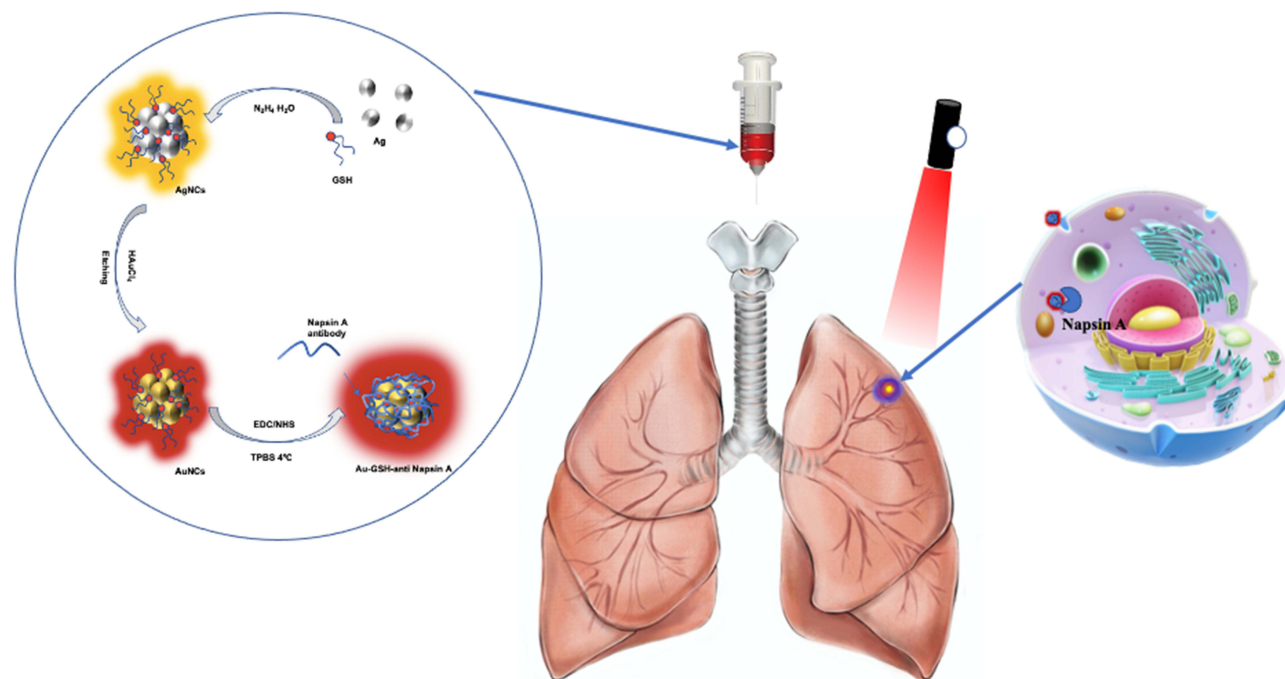
surgical approach for lung adenocarcinoma, owing to its advantages of minimal invasiveness and rapid recovery. In patients whose lesions were <15 mm in diameter and where the distance to the pleura was >10 mm, lesions were not detected during the surgery.[2] The current methods for pulmonary nodules localization: CT-guided markers localization, bronchoscopy markers localization, intraoperative ultrasound, 3D printing, intraoperative molecular imaging (IMI) and artificial intelligence (AI) assisted localization et al.[3] Due to the disadvantages of CT-guided percutaneous or broncho-scopy-guided placement of markers, IMI has become a hot research topic. ICG approved by FDA is widely used in clinical by venous injection. Due to the fast metabolism and poor specificity of intravenous injection of ICG, Quan et al first tested 6 patients using ICG by airway administration. The results showed that the fluorescence is located at the edge of the tumor and normal lung tissue, not inside the tumor.[4] Therefore, a new molecule which can make lung cancer recognized intraoperative by intratracheal delivery is needed.

Researchers have intensively investigated gold nanoparticles (AuNPs) in cancer diagnosis and treatment due to their inherent properties.[5,6] AuNPs, stable and non-immunogenic, have low toxicity.[7] They enable diagnostic imaging sensitivity and therapeutic efficacy through passive targeting, often referred to as enhanced permeability and retention (EPR) effect, or active targeting that can pass readily through the neovascularization of tumor tissue and the lymphatic system.[8–10] Gold nanoclusters (AuNCs) start to exhibit photoluminescence when the size is reduced to the sub-nanometer scale, while AuNPs have unique surface plasmon resonance optical properties.[11] Thus, AuNCs show great potential as optical visualizers. The fluorescence of AuNCs is determined by the intrinsic quantization effects of core and surface ligands.[12] Synthesized α-lactalbumin-stabilized AuNCs with three different emission wavelengths of 450 nm, 520 nm, and 705 nm, and used 705 nm AuNCs for in vivo fluorescence imaging of MDA-MB-231 and for fluorescence-guided surgery using AuNCs. The fluorescence of AuNCs is more stable than that of molecular dyes, making AuNCs more suitable than molecular dyes as fluorescent imaging agents. Jiang et al performed ^{89}Sr-labeled C6A-GSH@AuNCs to eradicate both the primary tumors and their lung metastases. Their study suggested that GSH-coated AuNCs held great promise for developing novel radiopharmaceuticals that specifically target the tumor acidic microenvironment for tumor diagnosis and treatments.[13] In contrast to the passive targeting of AuNCs described above, Pyo et al were able to

selectively bind folate receptor-positive cancer cells using FR binding to AuNCs and found that the folate moiety further enhanced the fluorescence quantum yield of AuNCs through energy transfer.[14] These studies confirm the great potential of AuNCs as fluorescent imaging agents for cancer diagnosis.

Aspartate protease A, Napsin A or NAPSA, TA01/TA02, is a 45 kDa single-chain protein and 420 amino acids encoded by the NASPA gene located on the long arm of chromosome 19, 13.33.[15] Napsin A expression is increased in pathological conditions including inflammatory disease and lung dysplasia and increased expression of Napsin A is also seen in the serum of patients with interstitial lung fibrosis, and its increase correlates with the severity of the disease.[16] One study of whole genome RNA sequencing combined with protein analysis in patients with non-small cell lung cancer identified 10 genes (including NAPSA) that qualified as promising biomarkers.[17] TTF-1, Napsin A, CK5/6, P63 and P40 are the most commonly used immunohistochemical markers for the classification of non-small cell lung cancer (NSCLC), and these markers have different sensitivities and specificities.[18] In contrast, it is not expressed or is lowly expressed in small cell carcinoma, large cell carcinoma, and pulmonary neuroendocrine tumors. Napsin A is regulated by TTF-1[19] and Napsin A negative is an independent indicator of poor overall survival prognosis in patients with lung adenocarcinoma.[20,21] Recently, it has also been shown that Napsin A is also a discovery tumor-associated self-antigen (DITAS) that induces Napsin A-specific CD8+ T-cell aggregation in blood and tumor tissue in patients applying tumor immune checkpoint blockade (ICB).[22] By assessing Napsin A levels in epithelial lining fluid (ELF), Uchida et al found that ELF levels were significantly higher on the adenocarcinoma side of the lung than on the contralateral side, with no difference between the two sides in non-adenocarcinoma patients and that Napsin A was significantly more altered than CEA. Therefore, it was demonstrated that Napsin A in ELF may become a new assay.[23]

In this study, Au-GSH-anti Napsin A nanoclusters (NapA-AuNCs) were synthesized, which were highly efficient, long residence in lung adenocarcinoma by airway administration. They had a good application prospect in the imaging and diagnosis of lung adenocarcinoma.

Materials and Methods
Materials
L-glutathione (L-GSH) was purchased from Aldrich; $HAuCl_4$ and $AgNO_3$ were of analytical grade and purchased from Sinopharm Chemical Reagent; N-(3-dimethylaminopropyl)-N′-ethylcarbodiimide hydrochloride (EDC, 98.5%) and N-hydroxysulfosuccinimide (NHS, 98%) were purchased from Aladdin; $N_2H_4.H_2O$ (85 wt%), NaOH, acetone, and isopropyl alcohol were of analytical grade and purchased from Beijing Chemical Works (China). Napsin A antibody was purchased from Santa Cruz biotechnology (USA). Calcein AM, PI, CCK-8, DAPI, Hoechst, 4% polyformaldehyde were purchased from Biosharp (China). Fetal bovine serum (FBS), Phosphate-buffered saline (PBS), Dulbecco's Modified Eagle medium (DMEM), penicillin–streptomycin solution (PS) and ethylene diamine tetraacetic acid (EDTA) solution were obtained from Gibco (USA). BEGM was purchased from Lonza (Switzerland). A549 ATCC cell lines and Beas-2b ATCC cell lines were purchased from Biomart (China). Eighty 5 weeks aged male BALB/cA-nu mice were purchased from Huafukang bioscience (China) and housed in a specific pathogen-free environment with free access to food and water and a quiet laboratory with a temperature range of 22–25°C and a humidity range of 50–60%, with alternating light and dark day and night. The animal experiments in this study were anesthetized by isoflurane and euthanized by overdosage CO_2.

Methods
Synthesis of NapA-AuNCs With Red Fluorescence
First, the AuNCs were prepared following a previously reported method.[24] Two milliliters of Au-GSH (AuNCs) solution at a concentration of 5 mg/mL was added with 7.2 mg EDC and 2.4 mg NHS. pH was adjusted to 6.5–7.0, activated and stirred for 15 min. Ten microliter of Napsin A antibody stock solution was added and shaken at 4°C for 8 h. The resulting product was dialyzed for 7 days at 4°C using a 3500 molecular weight dialysis bag. The dialyzed solution was lyophilized for use.

Mucus Penetration Assay

NapA-AuNCs and AuNCs (5 mg/mL, 200 μL) were separately added to the bronchial mucus simulant (BMS). The depth of penetration of NapA-AuNCs and AuNCs was observed in the EP tubes at different times.

Ten percent gelatin solution was configured and quickly spread to the bottom of tubes and slowly cooled to solidify. Then, add 1 mL of bronchial mucus simulant on top of the gelatin layer, and slowly add NapA-AuNCs and AuNCs (5 mg/mL, 200 μL) as the experimental groups; NapA-AuNCs added to gelatin as the positive control group; and PBS added to gelatin as the negative control group. The solution was aspirated after 24 hours in dark, and the gelatin was gently washed with PBS three times. The gelatin of each group was melted and added into 96-well plates, and the quantitative detection of mucus penetration was performed using small animal in vivo imaging system (IVIS).

Six BALB/cA-nu mice with A549 cell line-derived xenografts (CDX) model were given NapA-AuNCs or AuNCs (1:1) (5 mg/mL, 25 μL), then the mice were executed 15 minutes after intratracheal delivery. The tracheas of the mice were removed, and frozen slices were made. Confocal laser scanning microscopy (CLSM, Olympus, Fluoview FV1000) was used to observe mucus penetration in vivo.

In Vitro Cytotoxicity of NapA-AuNCs
CCK-8

A549 and Beas-2b cells were seeded in 96-well plates in DMEM and BEGM. The next day, the cells were treated with gradient concentrations of NapA-AuNCs. The A549 and Beas-2b cells were incubated with NapA-AuNCs and measured cell viability using the CCK-8 assay.

Calcein-AM/PI Staining Experiment

A549 and Beas-2b cells were seeded in 6-well plates, then treated with NapA-AuNCs (5 mg/mL, 600 μL) for 24 hours. The cells were cocultured with a double staining reagent (AM at 2×10^{-6} M and PI at 4×10^{-6} M) to distinguish between living and dead cells. The cells were visualized using fluorescence microscope.

Flow Cytometry

A549 and Beas-2b cells were seeded in 6-well plates. NapA-AuNCs was added and then incubated in the incubator for 24 hours. Apoptosis was detected using double staining reagent (AM at 2×10^{-6} M and PI at 4×10^{-6} M) by flow cytometry (Cytek Biosciences, USA).

Hemolysis Experiment

About 0.5 mL of different concentration gradients of NapA-AuNCs and 0.5 mL of 2% erythrocyte suspension were mixed. After being stood in a 37°C water bath for 3 h, 100 μL of supernatant was placed in a 96-well plate to measure the absorbance at 540 nm.

Fluorescence in vitro
Laser Confocal Imaging

A549 and Beas-2b cells were inoculated in confocal dishes with 5×10^4 cells in 3 mL overnight. NapA-AuNCs and AuNCs (5 mg/mL, 600 μL) were added to the confocal dishes and co-cultured for 12 h. Then, cells were observed under CLSM.

Fluorescence Intensity Curve

A549 cells were seeded in 96-well plates at a density of 3×10^3 cells per well in 100 μL of complete media and incubated overnight. NapA-AuNCs (5 mg/mL, 10 μL) was added in wells as the experimental groups. Ten microliter Hoechst and 10μL NapA-AuNCs were added to the 96-well plate, and the same field of the plate was photographed at different times using High Content System (PerkinElmer Operetta CLS™).

Tumor Spheres Penetration Assay

A549 cells inoculated into U-shaped ultra-low attachment 96-well plates at a density of 1500 cells/well for 5 days. When

the A549 cell spheres were 500 μm, NapA-AuNCs and AuNCs (5 mg/mL,10 μL) were added to the wells. The same field of view was photographed to observe fluorescence intensity at different times using PerkinElmer Operetta CLS™ to observe the mode and amount of AuNPs entering the tumor sphere versus time.

Cells Uptake Performance of NapA-AuNCs

A549 and Beas-2b cells were cultured. NapA-AuNCs and AuNCs (5 mg/mL,200 μL) were added to the 6-well plates and co-culture for 4 hours. Cell fluorescence intensity was detected by Flow cytometry (Cytek Biosciences, USA).

Cell Line-Derived Xenograft (CDX) Models in Lung Cancer

Subcutaneous CDX model: A549 cells were prepared (2×10^6 cells in 100 μL) and inoculated subcutaneously into the armpits of BALB/cA-nu mice (6 weeks). In situ injection CDX model: Mice were anesthetized by isoflurane. A549 cells were prepared, 10^6 cells in 100 μL of Matrigel (354248, Corning, USA) mixture, and inoculated 20 μL into the left 4th intercostal space. Pulmonary metastasis CDX model: A549 cells were prepared (10^6 cells in 100 μL) and 200 μL inoculated into tail vein. The process of the lung cancer in situ CDX modeling and testing is illustrated in Scheme 1.

Fluorescence in vivo

(1) Differences of fluorescence intensity between NapA-AuNCs and AuNCs in vivo: The subcutaneous model mice were divided into three groups (each group 5 mice): group 1, negative control group (PBS intravenous); group 2, AuNCs (5 mg/mL, 100 μL intravenous); group 3, NapA-AuNCs (5 mg/mL, 100 μL intravenous). Isoflurane anesthesia mice were performed at 0, 2, 4, 6, 8 hours after intravenously injection using IVIS.
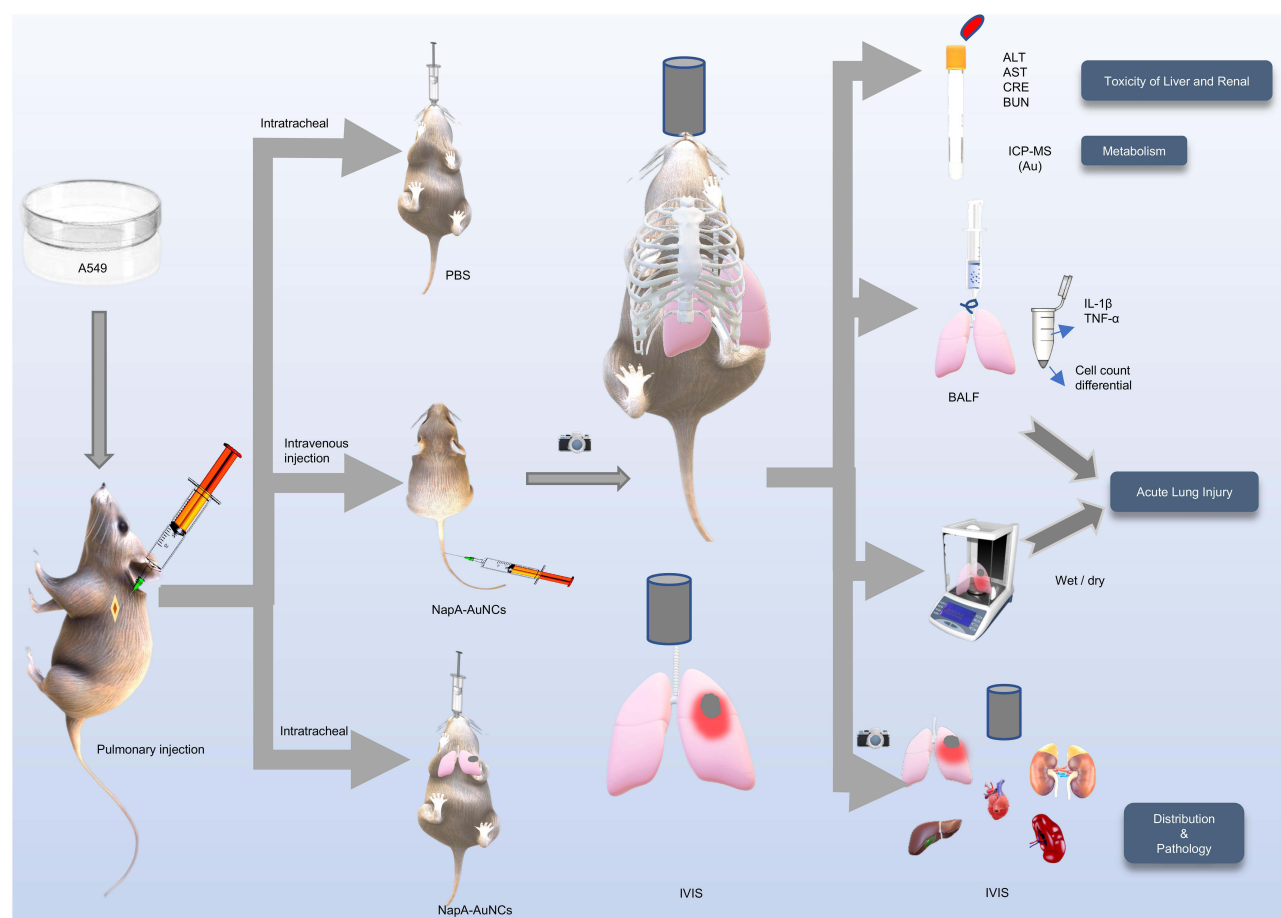
Scheme I Lung cancer in situ CDX modeling and testing.

(2) Fluorescence imaging of NapA-AuNCs intratracheal delivery: Lung cancer in situ model mice were divided into three groups: group 1 (5 mice), negative control group (PBS 25 μL intratracheal); group 2 (5 mice), NapA-AuNCs (5 mg/mL, 100 μL intravenous); group 3 (20 mice), NapA-AuNCs group (5 mg/mL, 25 μL intratracheal). IVIS imagings were performed in the above groups at 2, 4, 6, 12 hours after NCs administration. Group 2 mice were executed by excessive carbon dioxide after 6 hours of NapA-AuNCs administration. Group 3 mice were executed after imaging at different time points, and IVIS imaging (excitation 535 nm) of lungs were performed to observe the fluorescence imaging.

(3) All the 10 pulmonary metastasis model mice were intratracheal delivered 25 μL NapA-AuNCs. IVIS imaging of lungs (outside and inside surfaces) were performed 4 hours later.

NapA-AuNCs Distribution and Metabolism

The organs of the lung cancer in situ model mice that NapA-AuNCs (5 mg/mL, 25 μL) intratracheal and NapA-AuNCs (5 mg/mL, 100 μL) intravenous were removed 4 hours later, and the IVIS imaging was performed to observe the early distribution in the organs. The organs of the same model mice that NapA-AuNCs (5 mg/mL, 25 μL) intratracheal were removed 24 hours and 7 days later to observe the long-term distribution.

The same model 5 mice intravenously injected NapA-AuNCs (5 mg/mL, 200 μL) were taken 5 μL blood at different times. Then, blood was dissolved in aqua regia, and Au concentration was detected by ICP-MS to calculate the half-life of NapA-AuNCs in the blood.

In vivo Toxicity of NapA-AuNCs Intratracheal Administration

The blood of lung cancer in situ model 10 mice that NapA-AuNCs (5 mg/mL, 25 μL) intratracheal was taken 24 hours and 7 days later (1:1) to detect alanine transferase (ALT), aspartate transferase (AST), creatinine (CRE) and blood urea nitrogen (BUN). The organs were removed for pathology to observe acute and chronic toxicity. The same model 5 mice were undergone alveolar lavage to detect interleukin-1β (IL-1β), tumor necrosis factor-α (TNF-α) and cell counting stained with Richter-Gimza. Lung tissue of the same model mice took a constant weight and weighed again after drying at 60°C for 48 hours, then the wet-to-dry ratio was calculated.

Pathology

Tumors of subcutaneously mice, lungs of in situ lung cancer mice by intrapulmonary injection, and lungs of lung cancer metastatic mice by tail vein injection were removed for pathology photography, observation of tumorigenesis and measurement of tumor size and location. H&E sections and immunohistochemical (IHC) staining for Napsin A were observed by microscopy.

Results and Discussion
Synthesis and Characterization of NapA-AuNCs

The fabrication process of the novel NapA-AuNCs is illustrated in Scheme 2, aiming to achieve targeted recognition of lung adenocarcinoma cells. The morphology, size, distribution, and microstructure of NapA-AuNCs are characterized. Transmission electron microscopy (TEM) analysis revealed that AuNCs had a typical uniform spherical shape (Figure S1) and a narrow size distribution of 1.5–3.3 nm (Figure S2). After Napsin A antibodies were linked to AuNCs, NapA-AuNCs maintained a similar spherical structure as AuNCs (Figure 1a), but the size was 4.2–6.0 nm observed by TEM (Figure 1b). The hydrated diameter of NapA-AuNCs was 120 nm observed by DLS (Dynamic Light Scattering) (Figure 1c). NapA-AuNCs are significantly larger in size compared to AuNCs, which is considered to be caused by the fact that GSH on the surface of AuNCs can be linked to multiple Napsin A antibodies. The DLS hydration radius is larger than TEM because the long chains of gold clusters stretch in the aqueous solution. In addition, the zeta potential of NapA-AuNCs in aqueous suspension was positive at −32.2 mV, while the Napsin A displayed a positive charge at 6.5 mV. After Napsin A modification, NapA-AuNCs had an intermediate charge of −12.1 mV (Figure 1d), confirming the success of the Napsin A coating. The characteristic absorption peaks of C=O and N-H appeared at 1530 cm^{-1} and 1748 cm^{-1} in the IR spectrum of NapA-AuNCs complexes, respectively, indicating the amidation reaction, and the characteristic absorption peaks of the Napsin A antibody were also observed near −3500 cm^{-1}, which proved that the NapA-AuNCs complexes were successfully bound (Figure 1e). The UV-Vis was a broad absorption, and there was no characteristic absorption peak of large-sized nanoclusters (Figure 1f), which also
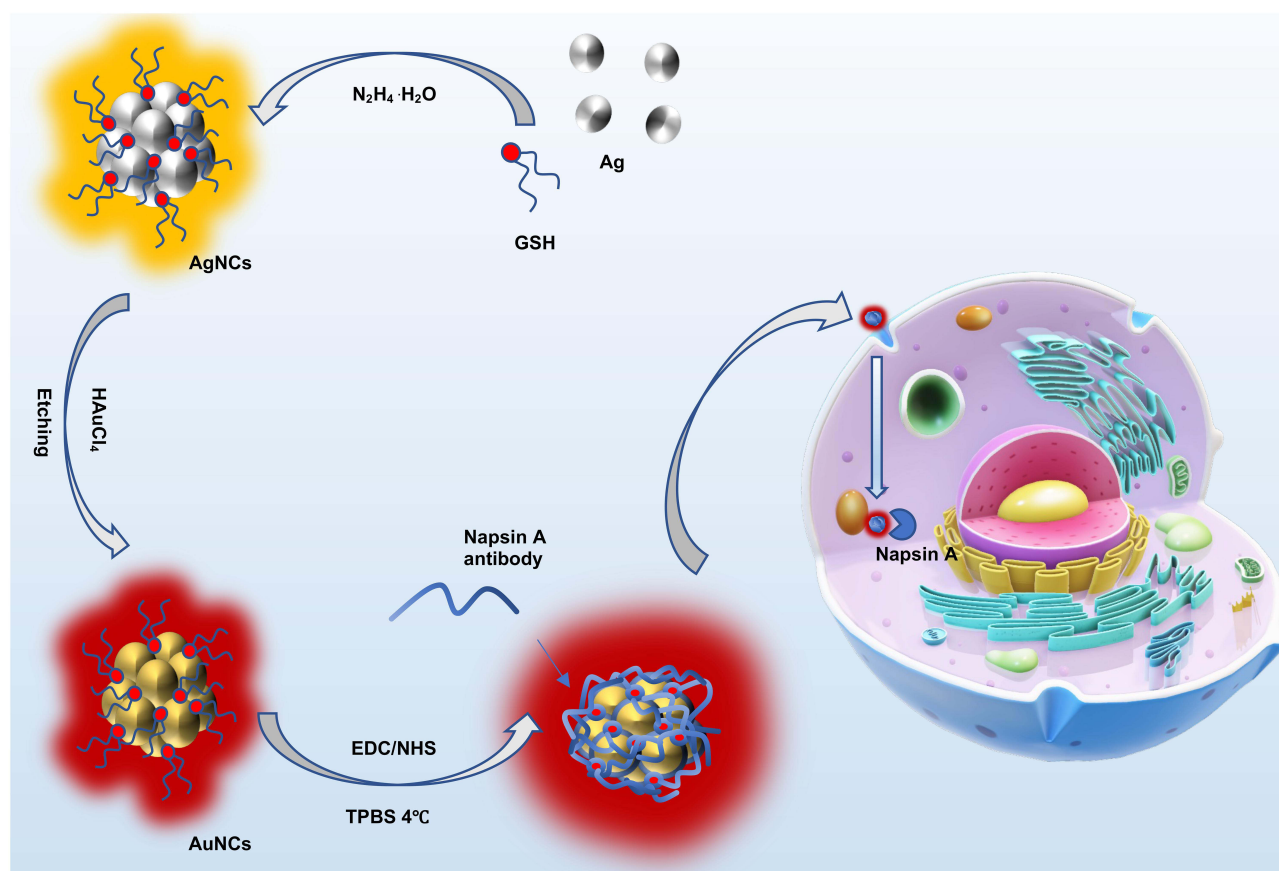
Scheme 2 Preparation of gold nanoclusters NapA-AuNCs and the major mechanism of fluorescence.

proves that the size of nanoclusters was small, which was consistent with the TEM results. The chemical composition and elemental valence states of AuNCs were indicated by X-ray photoelectron spectroscopy (XPS) measurements (Figure 1g). The electrochemical reduction reaction was verified by the appearance of two characteristic peaks at 88.5 eV and 84.5 eV for the 4f orbital binding energy of Au (Figure 1h), which demonstrated that Au(0) and Au(I) were contained in the AuNCs, and also showed that the high valence state of Au(III) could be reduced to Au nanoclusters by the electrochemical exchange reaction. The S 2p orbital binding energy at 164.9 eV and 163 eV also show two asymmetric characteristic peaks representing unbonded sulfhydryl compounds and gold sulfhydryl analogs formed by S elements and Au, respectively, which also demonstrates that through Au-S bonding, the GSH ligand is attached to the surface of gold nanoclusters, Au(0), and that not all of the sulfhydryl groups of GSH are riveted to the AuNCs. The characteristic absorption peak at 168.9 eV is also visible, also indicating that the AuNCs also have S elements in the oxidized state (Figure 1i).

Optical Properties of NapA-AuNCs

The incorporation of NapA-AuNCs has significantly enhanced their fluorescence imaging ability, resulting in an emission wavelength of 650 nm (Figure 2a). The stability of NapA-AuNCs was observed for 14 days, which showed excellent fluorescence stability, and no significant change in the intensity of the fluorescence spectrum was seen (Figure 2b). Under UV light at 365 nm, the results showed good fluorescence stability for 18 hours, a slight decrease in fluorescence intensity at 24 hours, the fluorescence intensity was still more than 2,500 a.u., and fluorescence bleaching did not occur with UV irradiation (Figure 2c). The fluorescence stability in different solutions (water, PBS, TPBS, saline, serum) and pH 4–10 was also tested, and the results showed that NapA-AuNCs displayed good fluorescence stability in different solutions and pH (Figure 2d and e). NapA-AuNCs have excellent fluorescence stability, and the reason considered is that
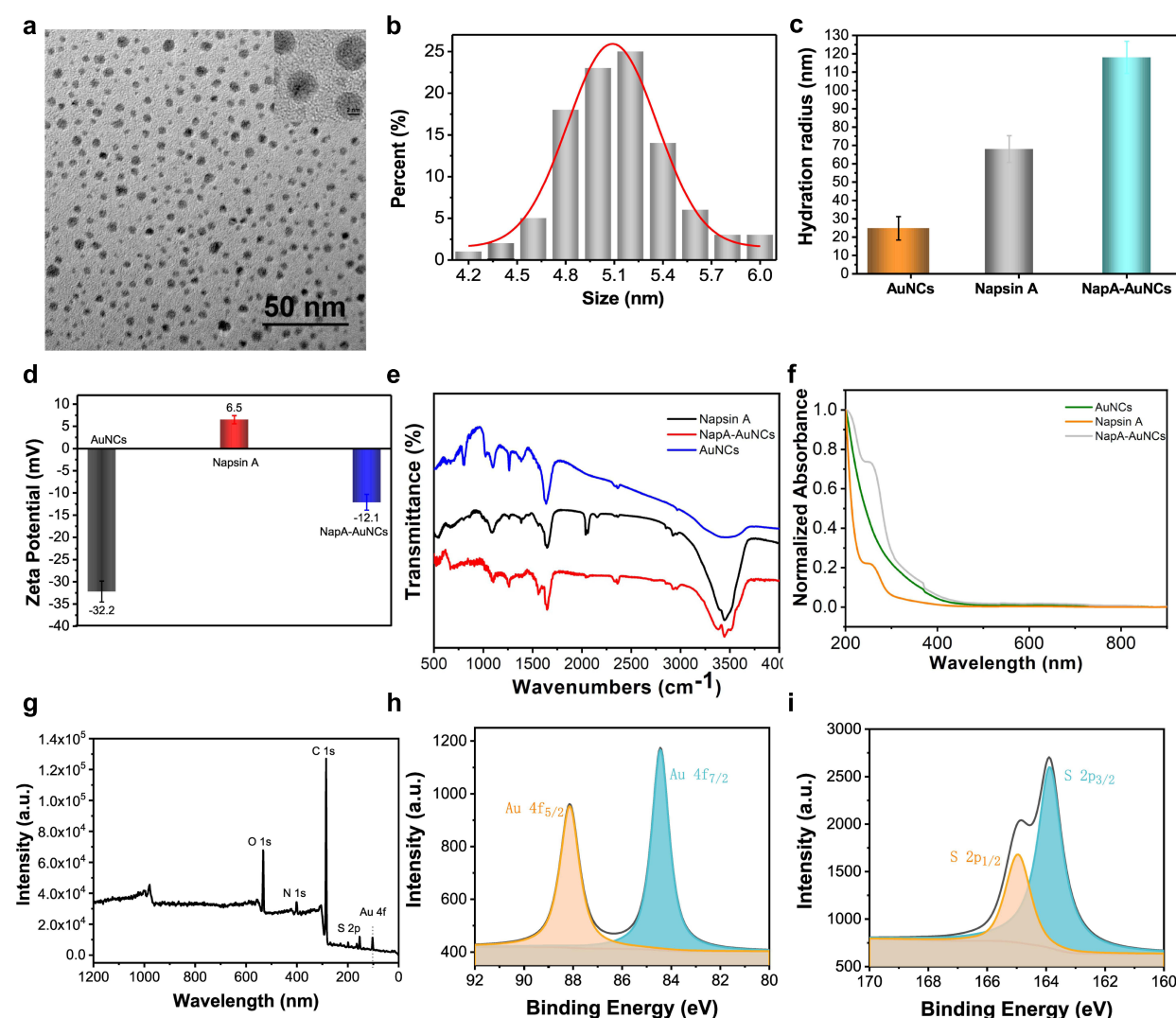
Figure 1 Characteristics of AuNCs and NapA-AuNCs. (**a**) TEM characteristics of NapA-AuNCs (scale bar: 50 nm), the small figure in the upper right corner is a local zoom-in (scale bar: 2 nm). (**b**) Normal distribution curves of NapA-AuNCs dimensions (100 nanoclusters measurement). (**c**) Hydration radius of AuNCs, Napsin A and NapA-AuNCs, the data exhibited as mean ± SD (n = 3). (**d**) Zeta potential of AuNCs, Napsin A and NapA-AuNCs.The data exhibited as mean ± SD (n = 3). (**e**) FTIR spectra of AuNCs, Napsin A and NapA-AuNCs. (**f**) UV-Vis spectrum of AuNCs, Napsin A and NapA-AuNCs. XPS of (**g**) AuNCs binding energy. (**h**) Au 4f binding energy. (**i**) S 2p binding energy.

the AuNCs have the protective effect of GSH ligands on the surface, which forms a protective layer to protect the carboxyl and amine functional groups inside the molecule from the external environment.[25]

Mucus Penetration Assay

The airway has a special barrier in the form of mucus, so NapA-AuNCs must have a strong penetration ability into mucus tissue to be able to perform subsequent in vivo experiments. BMS is currently more widely evaluated for in vitro penetration experiments by measuring the penetration depth of NPs. Results (Figure 3a) show that NapA-AuNCs and AuNCs can penetrate into mucus tissues as early as 1 hour in BMS, significantly after 3 hours, with essentially complete penetration after 12 hours. In the quantitative experiments, the melted gelatin was tested by IVIS and a significant difference can be seen between the experimental groups and control groups, while slight statistical difference between NapA-AuNCs and AuNCs (Figure 3b). In in vivo experiments, the distribution of AuNPs intratracheal delivery showed that both NapA-AuNCs and AuNCs aggregated in the tracheal mucus after 15 min of administration, and both of them had good penetration and even penetrated the epithelial cells of the trachea (Figure 3c). Mucus and cilia in the airway are
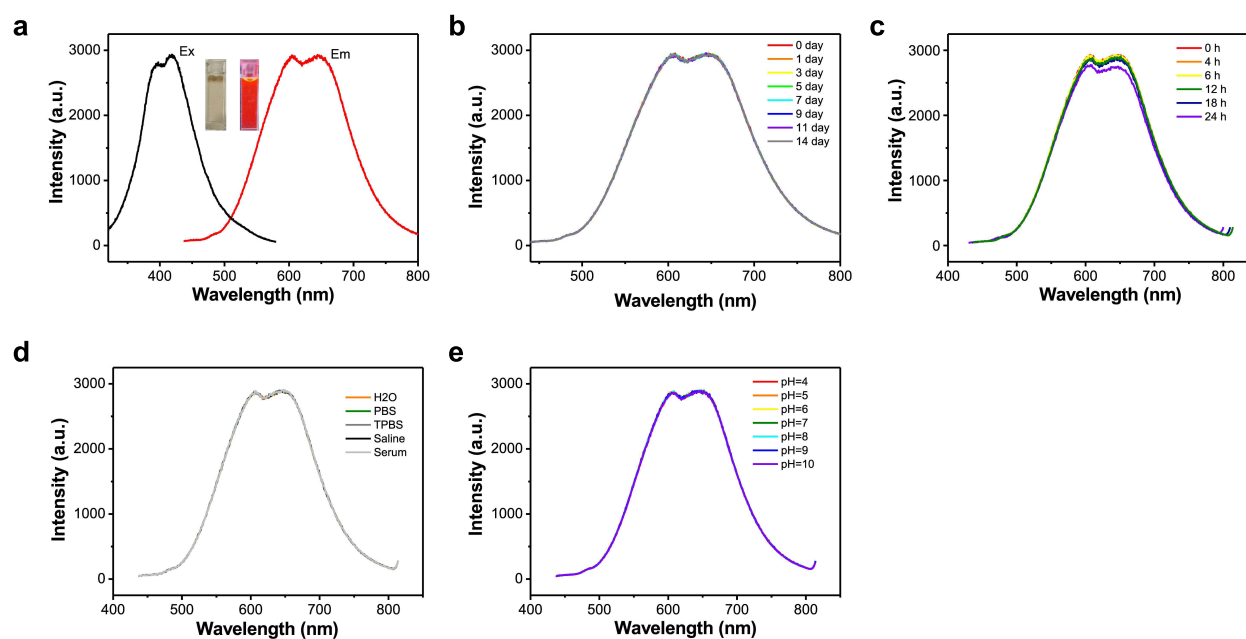
Figure 2 Optical properties of NapA-AuNCs. (**a**) Excitation and emission of NapA-AuNCs, the insets are photos under visible light and UV light. Fluorescence spectra of NapA-AuNCs (**b**) exposed to visible light at different times, (**c**) exposed to UV light at 365 V at different times, (**d**) in water, PBS, TPBS, saline and serum, (**e**) at pH 4–10.
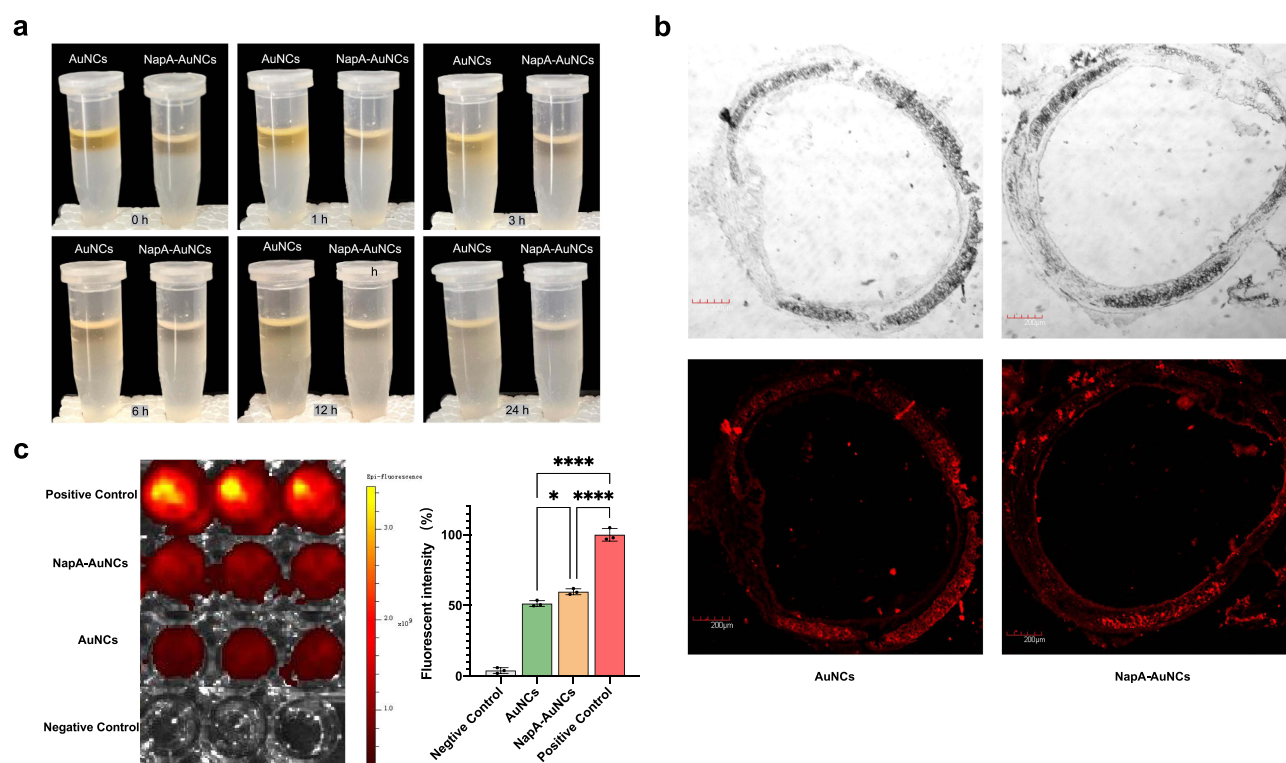

Figure 3 Airway mucus penetration experiments. (**a**) Penetration of NapA-AuNCs versus AuNCs in BMS at different times. (**b**) Fluorescence confocal visualization of NapA-AuNCs and AuNCs in mouse tracheal pathology sections (NapA-AuNCs and AuNCs in red, scale bar 200 μm). (**c**) Quantitative analysis of IVIS between NapA-AuNCs and AuNCs in BMS (Mean ± SD, n = 3; *p < 0.05, ****p < 0.0001).

the biggest challenges faced by nanomaterials. NapA-AuNCs can go through the mucosal barrier possibly due to: (1) small size of the nanoclusters. A research has shown that respiratory mucus is a viscoelastic solid on a macroscopic scale, and airway mucus has a reticular structure that is sufficiently small and viscous for NPs to penetrate NPs with diameters less than 100 nm can penetrate quickly.[26] (2) NapA-AuNCs have a negative charge. Suchaoin et al[27] observed the diffusion ability in the mucus layer by varying the zeta potential on the surface of the NPs and showed that the negatively charged self-emulsifying drug delivery system diffused faster in the mucus layer. The results of this experiment are consistent with all the above studies. However, in the quantitative analysis experiment, there was a significant difference in the experimental group compared to the positive control group, which may be due to the fact that the AuNPs were mixed well with the BMS after 24 hours and existed in the mixture, with limited gelatin-attached AuNPs.

In vitro Cytotoxicity of NapA-AuNCs

The cytotoxicity of NapA-AuNCs was evaluated in A549 cells and Beas-2b cells using CCK-8, Calcein-AM/PI staining, flow cytometry and hemolysis experiment methods. CCK-8 assay showed that different concentrations of NapA-AuNCs had a greater effect on the proliferation of A549 cells than Beas-2b cells, and the IC 50 value was much greater than 5 mg/mL (Figure 4a). The fluorescence microscopy results of live/dead cell staining measured with Calcein-AM/PI reagent are shown in Figure 4b. The results showed no statistical difference in the Beas-2b group co-cultured with NapA-AuNCs compared to the control group. However, there was a statistically significant difference in the A549 group compared to the control and Beas-2b groups with p-values of 0.032 and 0.007. The results of apoptosis measured using flow cytometry are shown in Figure 4c. The results showed that the toxic effect of NapA-AuNCs on Beas-2b cells was low, but the toxic effect on A549 cells was statistically significant with $p < 0.0001$. In the hemolysis experiment, the absorbance measurements at 540 nm were measured by aspirating the supernatant. A hemolysis rate >5% suggests that the nanomaterials may cause a hemolytic unsafe event. Our results suggest that NapA-AuNCs have good hemocompatibility and low hemolytic adverse safety events (Figure 4d). The results of cell viability and cytotoxicity in the A549 cell group compared to the Beas-2b cell group were both statistically significant. The reasons may be that the nanomaterials prepared in this experiment were small in size and GSH as a ligand. GSH is an important intracellular antioxidant, and the level of GSH is significantly higher in cancer cells compared to normal cells.[28] Au^{2+} and AuNPs can directly interact with GSH, leading to a decrease in GSH levels and thus depletion of GSH leading to cancer cell death.[29,30] Gao et al compared the extent of reduction in GSH levels induced by 8 nm and 37 nm AuNPs in human hepatocytes and demonstrated that smaller-sized AuNPs treated with AuNPs showed a greater reduction in GSH.[31] Another reason for A549 cells' high cytotoxicity is cancer cells uptake AuNPs increasingly. Cancer cells proliferate indefinitely due to excessive cell division caused by the lack of cell cycle control and apoptosis function.[32] The structure of glycoproteins expressed on the surface of their cell membranes is significantly different from that of normal cells,[33] leading to greater uptake of NPs by tumor cells. Therefore, when analyzing the mechanisms of cell viability and nanomaterial toxicity with cancer cells, the results may be completely different from normal cells.[34] This also validates the results of this experiment, where NapA-AuNCs co-cultured with A549 resulted in statistically significant apoptosis of cancer cells.

Fluorescence in vitro

The cells were observed after co-culture of 5 mg/mL NapA-AuNCs and AuNCs with A549 and Beas-2b cells for 24 h (Figure 5a), and the results showed that the fluorescence intensity was enhanced in the NapA-AuNCs co-culture group compared to the AuNCs group in A549 cells, p = 0.0273. The fluorescence intensity was increased in A549 cells compared to Beas-2b cells co-cultured with NapA-AuNCs, p = 0.0002. Fluorescence intensity of NapA-AuNCs co-culture with A549 cells at different times was observed (Figure S3), and the result showed that NapA-AuNCs entered the cells 1 hour after co-culture, and could reach a smooth and high fluorescence intensity after 2–8 hours, and the fluorescence slightly decayed after 10 hours and was still visible after 24 hours, but the intensity was significantly reduced (Figure 5b). U-shaped low-attachment plate allows the proliferating cells to grow into a sphere centered at the bottom. After observation of different heights of the sphere using PerkinElmer Operetta CLS™, it was found that both NapA-AuNCs and AuNCs were able to fluoresce from the edge to the center (Figures S4 and S5), and both could reach the center of the tumor after 4 hours of co-culture, and the fluorescence intensity was gradually enhanced with the
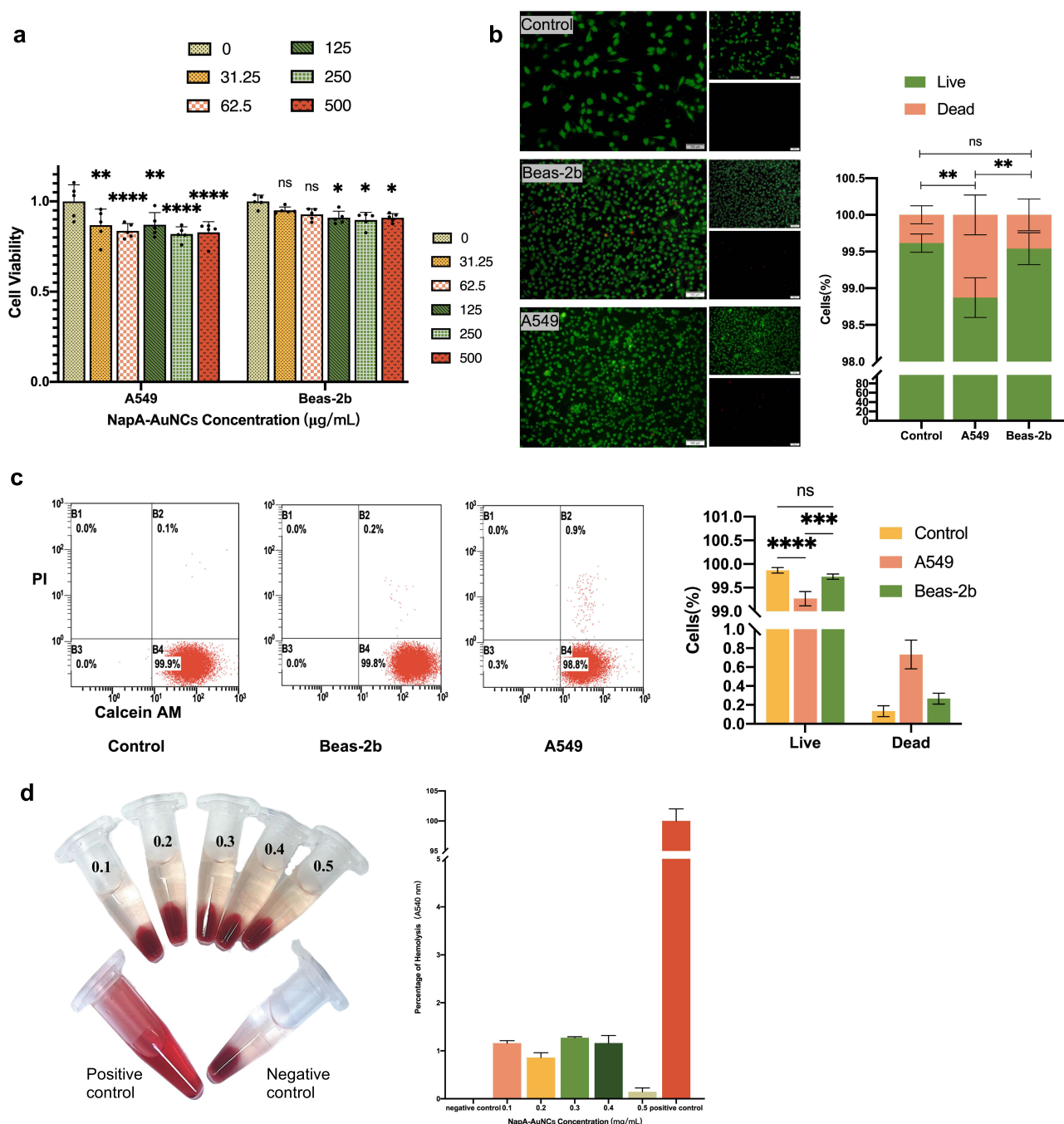
Figure 4 Cytotoxicity of NapA-AuNCs. (**a**) Cell viability assay (mean±SD, n=5, ns for no statistically significant, *p<0.05, **p<0.01, ****p<0.0001). A549 and Beas-2b were co-cultured with NapA-AuNCs (**b**) Calcein AM/PI staining fluorescence microscope images, green for live cells, red for dead cells (scale bar is 100 μm). Histogram of cell counts of live and dead cells after staining (mean ± SD, n=3, **p< 0.01) (Control group is A549 cells). (**c**) Apoptosis was detected by flow cytometry, and histograms were plotted (mean ± SD, n=3, ***p<0.001, ****p<0.0001) (Control group is A549 cells). (**d**) Hemolysis of NapA-AuNCs with different concentration gradients, and hemolysis rate (mean ± SD, n=3) was less than 5% (Positive control is erythrocyte with distilled water, and negative control is erythrocyte with PBS).

increase of time (Figure 5c). It has been shown that NPs with sizes less than 30 mm are more likely to penetrate into tumor tissues,[35] and NapA-AuNCs can bind to the target site and increase accumulation with time. The uptake pathways of NPs have been found to be phagocytosis, lattice protein-mediated endocytosis, follicular protein-mediated endocytosis, and non-lattice protein and non-follicular protein-mediated endocytosis.[36] Previous studies have shown that NPs can enter cells, nuclei, and cross the blood–brain barrier.[37] Size, shape, surface chemistry, roughness, surface coating, porosity, ligands, hydrophobicity and hydrophilicity are all likely to play a role in the membrane penetration effect.[38] The
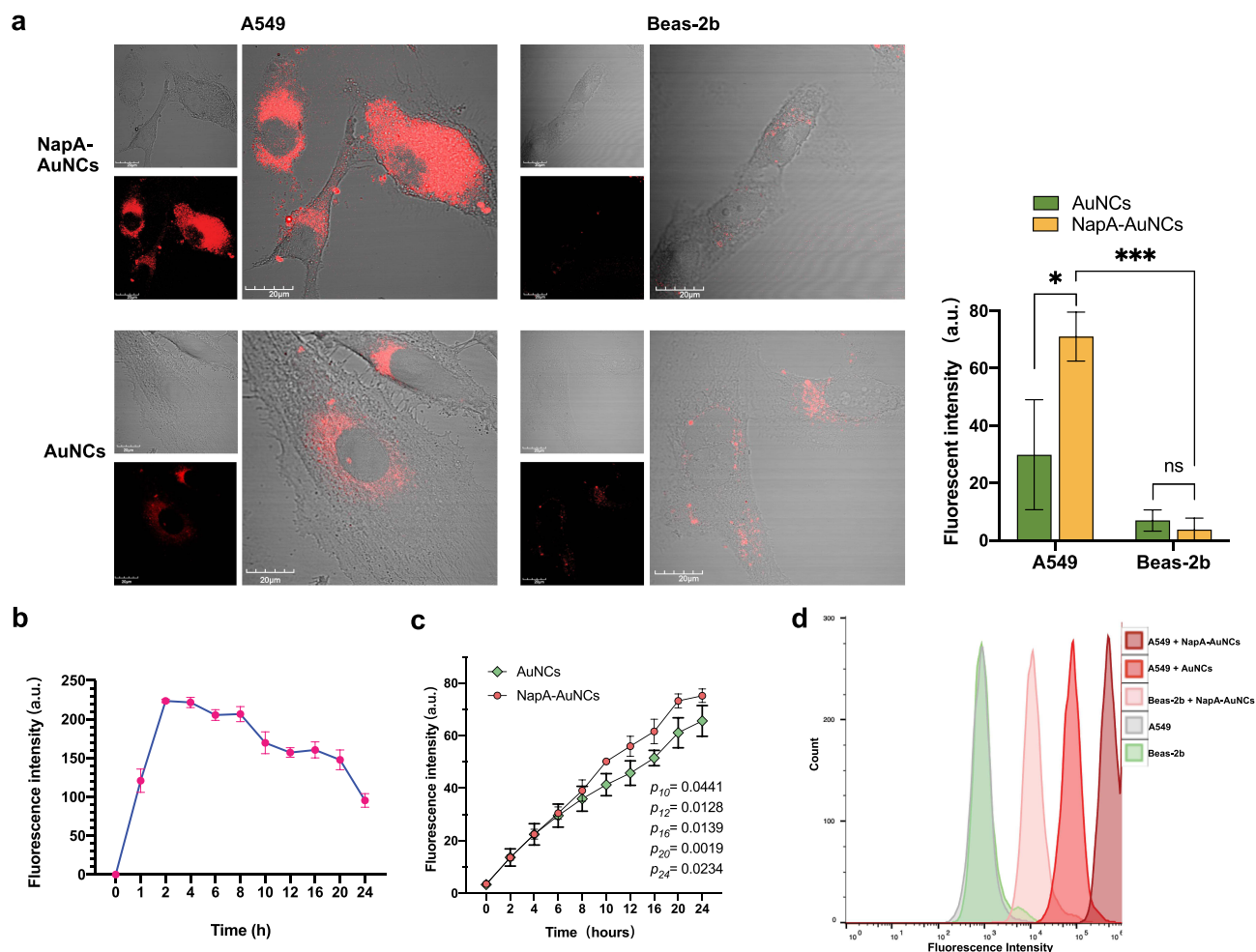
Figure 5 Fluorescence detection of NapA-AuNCs. (**a**) Fluorescence detection of A549 cells and Beas-2b cells co-cultured with NapA-AuNCs and AuNCs after 24 hours of co-culturing (scale bar: 20 μm) (mean ± SD, n=3, *p<0.05, ***p< 0.001). (**b**) Fluorescence intensity versus time curves for imaging of A549 cells co-culture with NapA-AuNCs for 24 h (mean ± SD, n=3). (**c**) Fluorescence intensity versus time curves of AuNCs, NapA-AuNCs co-cultured with A549 cell tumor spheres for 24 h (mean ± SD, n=3). (**d**) Fluorescence intensity of untreated cells, A549 cells and Beas-2b cells co-cultured with NapA-AuNCs, AuNCs.

shape and size of nanoparticles have a great influence on cellular uptake. Surface charge of NPs is another important influence on cellular uptake. The cell membrane surface carries a negative charge; however, negatively charged NPs can improve cellular uptake compared to uncharged NPs,[39] so it is also confirmed that the NapA-AuNCs prepared in this study have a negative charge on the surface, which also improves cellular uptake. NapA-AuNCs are considered mainly due to their small size and negatively charged surfaces, which allow them to enter the cell interior by passive transport via endocytosis and osmosis, and AuNPs coated with hydrophilic/hydrophobic ligands can penetrate the cell membrane without disrupting the cells.[40]

Cells Uptake Performance of NapA-AuNCs

The fluorescence intensity of cells uptake was observed using flow cytometry after co-culture for 4 h (NapA-AuNCs and AuNCs at a concentration of 5 mg/mL). The results showed that the fluorescence intensity of NapA-AuNCs co-cultured A549 cells was enhanced compared with the control groups and Beas-2b cells groups (Figure 5d). The stronger fluorescence intensity of A549 cells compared to Beas-2b cells may be due to: (1) increased uptake of NPs by cancer cells. (2) NapA-AuNCs lung adenocarcinoma-targeted. Most of the previous study targets are transmembrane proteins that are able to actively transport NPs into the cell via receptor-mediated cytosis. However, as proteins localized in the cytoplasm, few studies have investigated them as targets for nanomaterials. The NapA-AuNCs prepared in this study are Napsin A targeted, Napsin A present in the cytoplasm binds to the antibody at the end of NapA-AuNCs, which can

display fluorescence better and stay longer. NapA-AuNCs enter the cells half an hour after co-culture, and can reach the peak in 2–8 hours, and fluorescence could still be seen after 24 hours. The results of this study show that cytoplasmic protein localization also has its advantageous role.

Fluorescence in vivo

Fluorescence Imaging of Subcutaneous CDX Model

The AuNCs and NapA-AuNCs groups could reach a stable and bright red light after 6 hours of injection. And the fluorescence was significantly enhanced in the NapA-AuNCs group compared with the AuNCs group (Figure S6). It proved that NapA-AuNCs could enhance the fluorescence imaging of tumor.

Fluorescence Imaging of Lung in situ Injection CDX Model

The results showed that regardless of the administration method, in vivo imaging of the mice showed no specific fluorescence at the body surface, and the fluorescence at the chest wall was considered as surgical incision scars. The intratracheal group showed faster absorption and better specificity than the intravenous group, with stable accumulation at the lung tumor in 4 hours (Figure 6a). Former studies have shown that only 0.7% of the nanoparticle dose administered intravenously is delivered to solid tumors and that nanomaterial delivery is the least efficient for lung tumors.[41] However, the results of our study were different. The reasons for this were considered to be (1) passive transport: tumor tissues, due to their structural peculiarities (high vascular density, defective vascular structure, and impaired lymphatic reflux) and microenvironment (significantly more metabolically active than normal tissues and acidic environment),[42,43] can be damaged by the enhanced permeation retention effect (EPR). This passive approach provides many opportunities for NPs to enter the tumor. NapA-AuNCs are highly tumor permeable due to their ultra-small size, surface GSH ligands, and negative charge, anti-serotonin effect (essentially no effect with serum proteins that are also negatively charged), and long circulating lifespan that increases the chances for NPs to accumulate in the tumor.[41] Cabral et al[44] compared the accumulation effect of different sizes of long-circulating, drug-carrying polymer micelles (30–100 nm in diameter) in highly permeable and low-permeable tumors, and only 30 nm micelles could penetrate poorly permeable pancreatic tumors. (2) Active transport: recently, Warren Chan's team[9,10] disproved the nearly 30-year theory that NPs enter tumor tissues through the interstitial space of vascular endothelial cells. The transport of NPs that the primary mechanism of NPs transport is an active process rather than a passive one. This active process is a transendothelial mechanism mediated by vesicular apparatus formed by transporting endothelial cells (N-TECs). Berner's team[22] showed that Napsin A, a lung tumor-associated self-antigen, accumulates increased on the surface of lung cancer tissues. It has also been demonstrated that there is an elevation of Napsin A in the lung epithelial lining fluid assay in lung adenocarcinoma patients.[23] The NapA-AuNCs in our study have the effect of targeting Napsin A. Napsin A is enriched in lung adenocarcinoma, so the targeting material with antibodies against Napsin A can form an antigen–antibody complex with it and enhance its fluorescence intensity. Currently, inhalation delivery is mostly used for drug treatment, and it has been shown that the size of the nanomaterials is critical in influencing whether they can escape from alveolar macrophages,[45] thus improving therapeutic efficacy. Apart from reaching the lung parenchyma, the (bio)degradable nano-architectures are able to translocate as well to secondary organs and be almost completely excreted within 10 days.[46] The results of animal experiments in this part also verified the results above that NapA-AuNCs with a negatively charged surface and a molecular weight of 45 kDa can penetrate the mucosal barrier, escape capture by alveolar macrophages, rapidly enter the tumor tissue and exist for a longer period of time. Moreover, intratracheal showed faster and brighter fluorescence than intravenous.

The tail vein injection pulmonary metastatic CDX model was loaded with a total of 10 nude mice, one died after injection due to tail vein injection too rapidly, and lung cancer nodules of different sizes and locations were visible in the lungs of some of the mice after 7 days (Figure S7). The lung in situ injection method has confirmed that bright fluorescence can be seen at lung adenocarcinomas 4 hours after airway administration, we executed the l pulmonary metastatic CDX model mice 4 hours after airway administration of NapA-AuNCs, and the outside and inside surfaces of lungs were subjected to IVIS. The experimental results (Figure 6b) observed that strong fluorescence was visible at some hilars, and bright red fluorescence could be observed in lung cancer nodules (regardless of size) identified in the lungs,
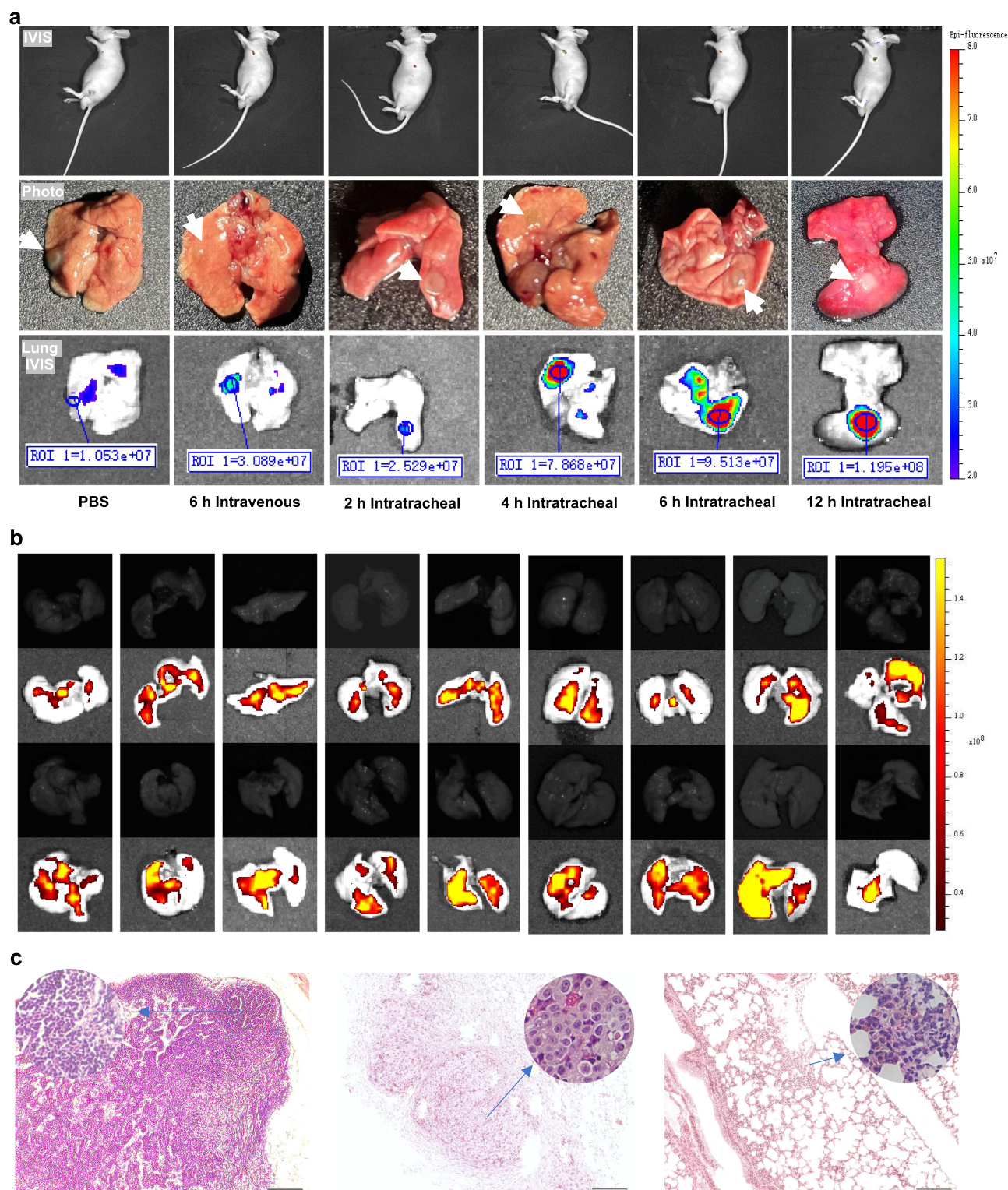
Figure 6 Fluorescence pathology. (**a**) Fluorescence localization of NapA-AuNCs in lung adenocarcinoma: the lung adenocarcinoma (white arrows) IVIS images in different time intratracheal points and 6 hours after intravenous administration. (**b**) Fluorescence IVIS Images of isolated lung tissues of lung cancer metastasis CDX model mice after intratracheal NapA-AuNCs for 4 hours (each column shows one mouse the photographs and IVIS fluorescence images of reversible sides of the same lung tissue). (**c**) H&E sections (×100) of tumors with different CDX models. The left panel shows a CDX model tumor with subcutaneous injection; the middle panel shows a CDX model tumor with intrapulmonary injection; and the right panel shows a CDX model tumor with vein injection. The upper right inset is a partial enlargement of the H&E section (×400) (scale bar: 200 μm).

and the closer the nodule was to the pleura, the stronger the fluorescence was. In some of the lung tissues, no obvious lung nodules were observed in the lungs, but red fluorescent areas were seen on IVIS imaging. When sampling in depth according to the area of fluorescence visualization, lung lesions could be seen. Co-registration of fluorescent NPs with lung morphology revealed significant differences in pulmonary NP distribution depending on the means of application (intratracheal instillation and ventilator-assisted aerosol inhalation under anesthetized conditions). Inhalation exhibited a more homogeneous NP distribution in conducting airways and acini indicated by a central-to-peripheral (C/P) NP. After inhalation, most NPs were observed in the proximal part of the acini as predicted by computational fluid dynamics simulations.[47] In terms of intraoperative fluorescence imaging, Quan et al[4] showed that tumor tissues as small as 0.2 cm and as deep as 0.5 cm could be detected after inhalation of ICG for 1 hour. ICG can identify tumor after intravenous, but the inhalation method can reverse the phenomenon for lung tumors, which means that the tumor is non-fluorescent and the rest of the lung tissue is uniformly green. Our study is not consistent with the results of Quan's. Considerable reasons may be that ICG can enter the blood circulation quickly after airway administration and has a short half-life, stays in the body for a short period of time, and is quickly excreted by the liver. In contrast, NapA-AuNCs have the advantage of a long residence time in the body, and enter the pulmonary vasculature more quickly after ventilator-assisted aerosol inhalation under anesthetized conditions, which allows them to enter the tumor tissue quickly and emit fluorescence.

Pathology was observed in different ways of CDX (Figure 6c). The subcutaneous CDX tumors were stained with H&E staining, which showed obvious cellular heterogeneity of the tumor tissue, local neovascularization, inflammatory cell infiltration and necrosis. In lung cancer in situ CDX tumors, 0.5 cm lung cancers could be seen in the lungs, and the results of H&E staining showed that some of the tumor cells were growing close to the wall, with obvious heterogeneity, dense arrangement, and tumor necrosis. Scattered clusters of cancer in the lungs could be observed after the fluorescent areas were sampled from isolated lung tissues of mice with lung cancer metastases CDX through IVIS imaging. NapA-AuNCs distribution and metabolism.

IVIS results on the distribution of NapA-AuNCs in different routes of administration showed that NapA-AuNCs were distributed in lung cancer tissues, kidneys and livers at an early time. NapA-AuNCs were excreted in the bile and urine. Compared with the intravenous group, the intratracheal group showed high accumulation in the lungs and small deposition in the kidneys (Figure 7a). Results of IVIS observations of the long-term distribution showed that 24 hours after intratracheal delivery, NapA-AuNCs were distributed mainly in kidneys and livers, while 7 days later only distributed on livers (Figure 7b). Au concentration was detected in ICP-MS, it showed the half-life of NapA-AuNCs is 23.59 hours (95% CI, 22.47–24.84) (Figure 7c). Koshkina et al[48] found that the dose of inhaled p53 plasmid was 1/5 of that given intravenously, and the area under the curve for intratracheal was 2.8 times that following intravenous way, with higher concentrations in the lungs. Organ deposition for intravenous administration was liver > spleen > blood ≥ lungs > heart > kidneys, while for intratracheal administration it was: lungs > heart > blood > spleen > liver > kidneys. As for metabolism, our study showed that the vast majority of NapA-AuNCs were metabolized by the liver and a small portion via the kidney, with very low deposition in the spleen and heart. Compared with intravenous administration, the intratracheal group had high pulmonary accumulation, low renal deposition and little effect on other organs.

In vivo Toxicity of NapA-AuNCs

We found that there were no changes on liver and kidney blood markers by testing ALT, AST, CRE and BUN after NapA-AuNCs intratracheal 24h and 7d. All the groups showed no statistical difference (Figure 8a and b). The IL-1β and TNF-α assays were tested in alveolar lavage. The p-values were 0.0706 and 0.052. Edema is one of the most important manifestations of acute lung injury, and a significant reduction in the lung wet-to-dry ratio could be seen. The results of this experiment showed no significant difference in the lung wet-to-dry ratio, with a p-value of 0.3413. Cell counts were performed on BALF, and the NapA-AuNCs group showed a slight increase in the total number of leukocytes compared to the control group with similar percentages of neutrophils, lymphocytes, and macrophages, and none of them were statistically significant (Figure 8c). 24 hours and 7 days after the NapA-AuNCs were intratracheal delivered, the hearts, livers, spleens, lungs, and kidneys were taken and stained for H&E, and the results showed no pathological changes (Figure 8d). NapA-AuNCs are mainly metabolized by the liver and kidney. In the study of in vivo toxicity, the metabolic pathways were mainly evaluated for hepatic and renal toxicity as well as pulmonary toxicity after intratracheal delivery. ALT and AST are the rapid assessment indicators of hepatic injury, and CRE and BUN are the assessment indicators of renal injury. The results of the study are
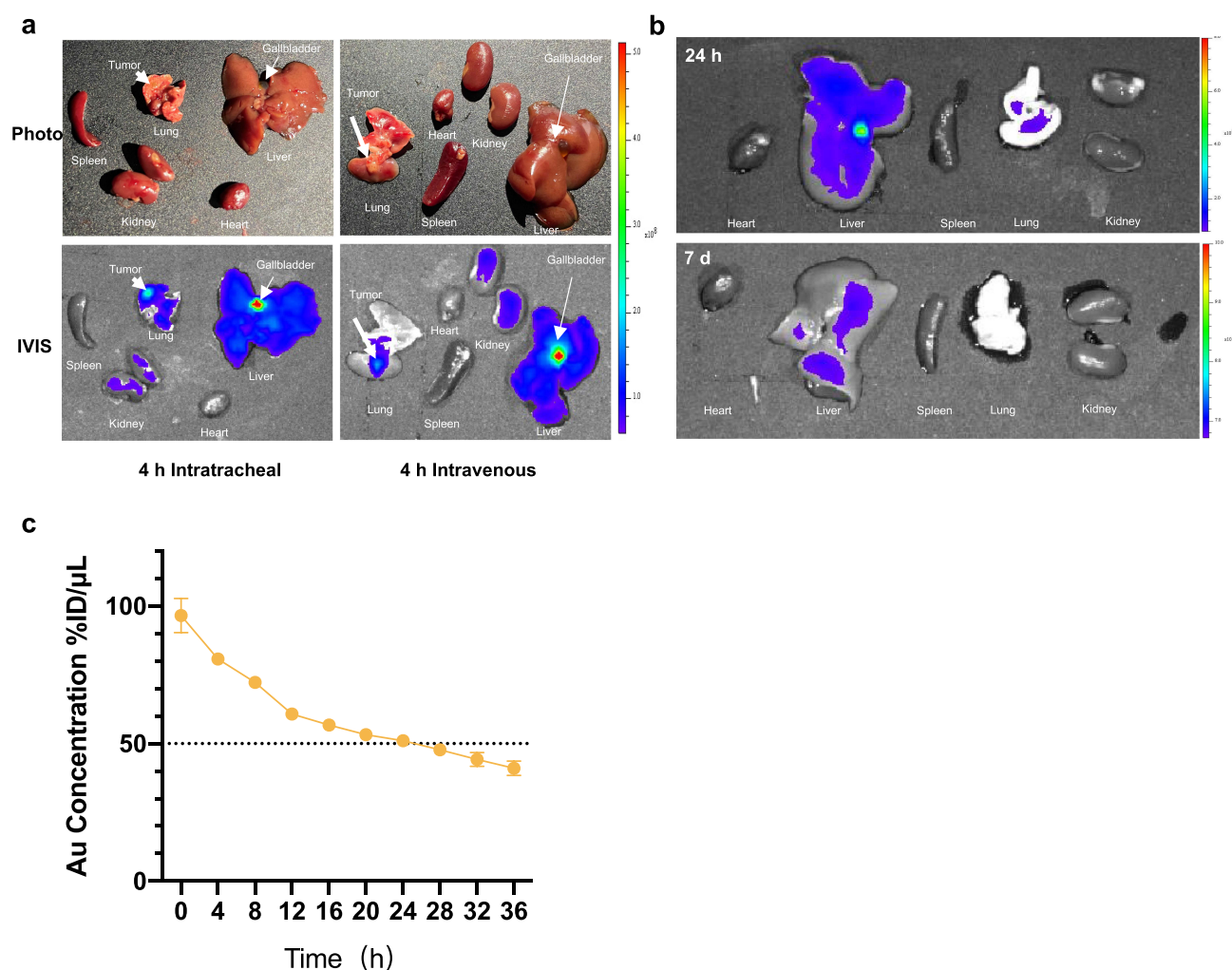
Figure 7 Distribution and metabolism of NapA-AuNCs. (**a**) IVIS fluorescence images of various organs (thick arrows are lung cancer tissues, thin arrows are gallbladder) 4 hours after NapA-AuNCs were administered. (**b**) IVIS Fluorescence Imaging of various organs 24 hours and 7 days after NapA-AuNCs intratracheal. (**c**) Detection of Au concentration in blood by ICP-MS after vein injection of NapA-AuNCs at 0, 4, 8, 12, 16, 20, 24, 28, 32, and 36 hours (mean ± SD, n=5).

similar to those of the majority of the studies on AuNPs and obtained a good liver and kidney safety.[49–52] IL-1β and TNF-α are sensitive indicators of the early stages of pneumonic disease, followed by changes in cellular components such as airway neutrophils, etc. TNF-α is an essential cytokine in the inflammatory and fibrotic response of the lungs after the presence of toxins, which initiates cell death and triggers alveolar epithelial dysfunction in acute lung injury. IL-1β and IL-6 are key mediators of the inflammatory response, and they are implicated in a wide range of cellular activities, including cell multiplication, division, and apoptosis.[53,54] The leukocyte counts in BALF with the classification of IL-1β, IL-1β, TNF-α and pulmonary edema were not statistically significant when looking at all the indicators. The results of H&E staining of organ pathology tissues show that there were no obvious pathological changes in all other organs, but the lung tissues can be seen to have mild edema in all of them, as well as in the PBS control group. It was considered that the cause could be caused by the mechanical irritation of the inner wall of the tube due to repeated use of anesthetic drugs in a short period of time and rapid airway drug delivery. Since there was no significant change in the experimental group compared to the control group, it was determined that NapA-AuNCs were safe for airway administration in animals.

Conclusion

In summary, airway administration of NapA-AuNCs is a safe, effective, and rapid intraoperative localization modality, and therefore the study intends to apply this noninvasive, targeted, rapid, and low-toxicity modality to the clinic to
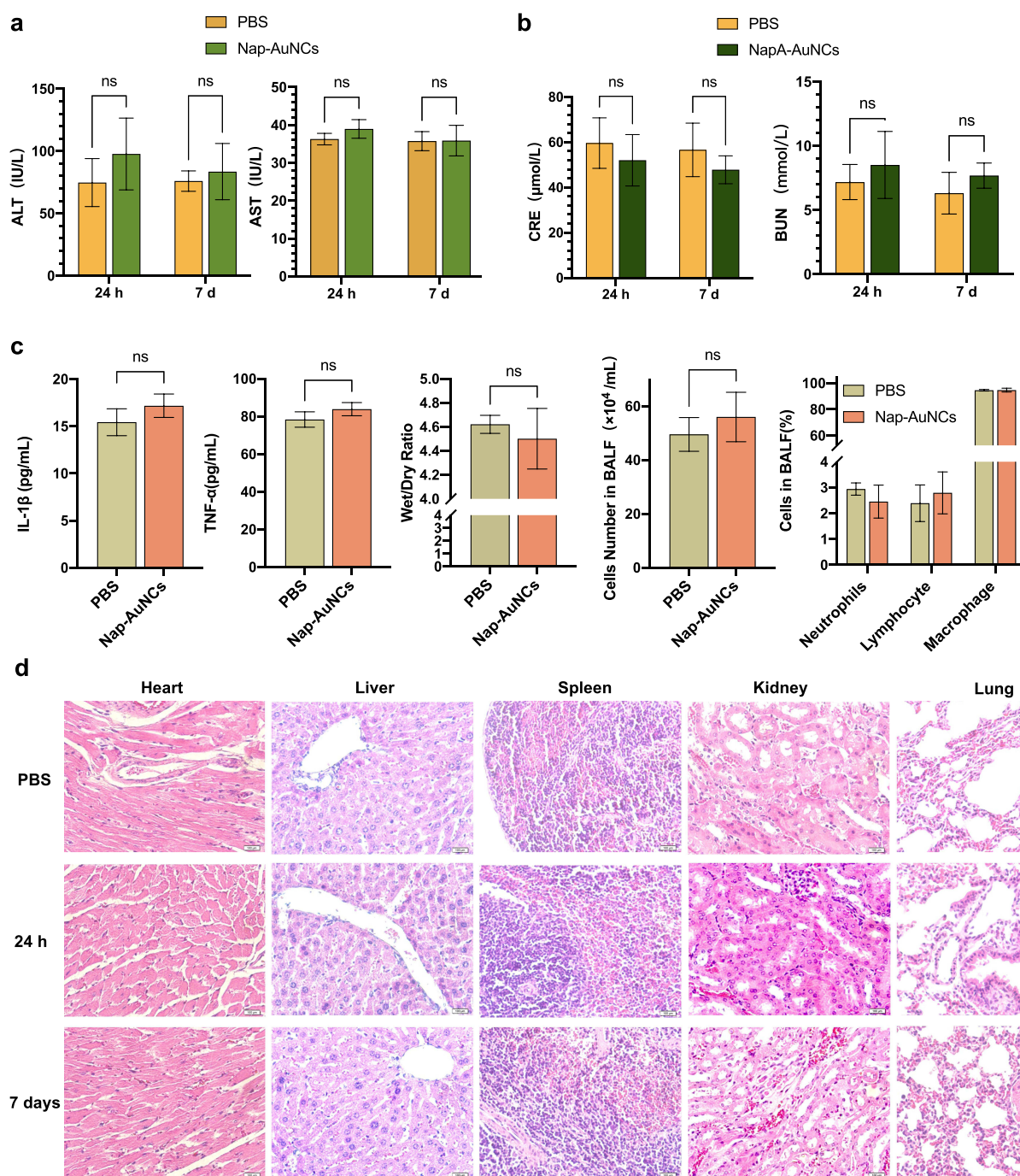
Figure 8 In vivo toxicity testing of NapA-AuNCs. (**a**) Liver function tests (mean ± SD, n=5). (**b**) Renal function tests (mean ± SD, n=5). (**c**) Pulmonary toxicity assay (mean ± SD, n=5). (**d**) H&E sections (×400) of different organ pathologies (scale bar 100 μm).

provide a better choice of strategies for intraoperative localization of lung adenocarcinoma, which has a certain prospect of application.

Abbreviations

NapA-AuNCs, Napsin A nanoclusters; CT, computed tomography; MITS, minimally invasive thoracic surgery; VATS, video-assisted thoracoscopic surgery; AuNPs, gold nanoparticles; EPR, enhanced permeability and retention; L-GSH, L-glutathione; BMS, bronchial mucus simulant; IVIS, in vivo imaging system; CDX, cell line-derived xenografts;

CLSM, confocal laser scanning microscopy; ALT, alanine transferase; AST, aspartate transferase; CRE, creatinine; BUN, blood urea nitrogen; IL-1β, interleukin-1β; TNF-α, tumor necrosis factor-α; IHC, immunohistochemical; TEM, transmission electron microscopy; DLS, dynamic light scattering; XPS, X-ray photoelectron spectroscopy.

Data Sharing Statement

All data generated or analysed during this study are included in this published article [and its supplementary information file].

Ethics Approval and Informed Consent

The animal experiments were approved by the Animal Welfare Ethics Committee of of the College Basic Medicine, Jilin University (2023219), following the Laboratory animal - Guideline for ethical review of animal welfare (GBT 35892-2018).

Acknowledgments

Assistance with the study: Thanks to Yucheng Zhang, Chenfei Kong from China–Japan Union Hospital of Jilin University Research center.

Author Contributions

All authors made a significant contribution to the work reported, whether that is in the conception, study design, execution, acquisition of data, analysis and interpretation, or in all these areas; took part in drafting, revising or critically reviewing the article; gave final approval of the version to be published; have agreed on the journal to which the article has been submitted; and agree to be accountable for all aspects of the work.

Funding

Disclosure

The authors declare that they have no competing interests in this work.

References

1. Mazzone PJ, Lam L. Evaluating the patient with a pulmonary nodule: a review. *JAMA J Am Med Assoc*. 2022;327(3):264–273. doi:10.1001/jama.2021.24287
2. Tamura M, Oda M, Fujimori H, Shimizu Y, Matsumoto I, Watanabe G. New indication for preoperative marking of small peripheral pulmonary nodules in thoracoscopic surgery. *Interact Cardiovasc Thorac Surg*. 2010;11(5):590–593. doi:10.1510/icvts.2010.241018
3. Tang L, Zhang Y, Wang Y. Intraoperative identification of pulmonary nodules during minimally invasive thoracic surgery: a narrative review. *Quant Imaging Med Surg*. 2022;12:5271–5287. doi:10.21037/qims-22-309
4. Quan YH, Oh CH, Jung D, et al. Evaluation of intraoperative near-infrared fluorescence visualization of the lung tumor margin with indocyanine green inhalation. *JAMA Surgery*. 2020;155(8):732–740. doi:10.1001/jamasurg.2020.1314
5. Gong F, Yang NL, Wang XW, et al. Tumor microenvironment-responsive intelligent nanoplatforms for cancer theranostics. *Nano Today*. 2020;32:100851. doi:10.1016/j.nantod.2020.100851
6. Wang Z, Ren X, Wang D, et al. Novel strategies for tumor radiosensitization mediated by multifunctional gold-based nanomaterials. *Biomater Sci*. 2023;11(4):1116–1136. doi:10.1039/D2BM01496C
7. Lee KX, Shameli K, Yew YP, et al. Recent developments in the facile bio-synthesis of gold nanoparticles (AuNPs) and their biomedical applications. *Int J Nanomed*. 2020;15:275–300. doi:10.2147/IJN.S233789
8. Donahue ND, Acar H, Wilhelm S. Concepts of nanoparticle cellular uptake, intracellular trafficking, and kinetics in nanomedicine. *Adv Drug Deliv Rev*. 2019;143:68–96. doi:10.1016/j.addr.2019.04.008
9. Sindhwani S, Syed AM, Ngai J, et al. The entry of nanoparticles into solid tumours. *Nature Mater*. 2020;19(5):566. doi:10.1038/s41563-019-0566-2
10. Kingston BR, Lin ZP, Ouyang B, et al. Specific endothelial cells govern nanoparticle entry into solid tumors. *Acs Nano*. 2021;15(9):14080–14094. doi:10.1021/acsnano.1c04510
11. Liu Z, Luo L, Jin R. Visible to NIR-II photoluminescence of atomically precise gold nanoclusters. *Adv Mater*. 2024;36(8).
12. Zhong Y, Zhang J, Li T, et al. Suppression of kernel vibrations by layer-by-layer ligand engineering boosts photoluminescence efficiency of gold nanoclusters. *Nat Commun*. 2023;14(1).
13. Jiang Y, Wu Q, Hou M, et al. pH-sensitive gold nanoclusters labeling with radiometallic nuclides for diagnosis and treatment of tumor. *Mater Today Bio*. 2023;19.

14. Yucel O, Sengelen A, Emik S, Onay-Ucar E, Arda N, Gurdag G. Folic acid-modified methotrexate-conjugated gold nanoparticles as nano-sized trojans for drug delivery to folate receptor-positive cancer cells. *Nanotechnology*. 2020;31(35):355101. doi:10.1088/1361-6528/ab9395

15. Weidemann S, Boehle JL, Contreras H, et al. Napsin A expression in human tumors and normal tissues. *Pathol Oncol Res*. 2021;27.

16. Samukawa T, Hamada T, Uto H, et al. The elevation of serum napsin A in idiopathic pulmonary fibrosis, compared with KL-6, surfactant protein-A and surfactant protein-D. *BMC Pulm Med*. 2012;12:12. doi:10.1186/1471-2466-12-12

17. Lindskog C, Fagerberg L, Hallstrom B, et al. The lung-specific proteome defined by integration of transcriptomics and antibody-based profiling. *FASEB J*. 2014;28(12):5184–5196. doi:10.1096/fj.14-254862

18. Kriegsmann K, Cremer M, Zgorzelski M, et al. Agreement of CK5/6, p40, and p63 immunoreactivity in non-small cell lung cancer. *Pathology*. 2019;51(3):240–245. doi:10.1016/j.pathol.2018.11.009

19. Ordonez NG. Napsin A expression in lung and kidney neoplasia: a review and update. *Adv Anat Pathol*. 2012;19(1):66–73. doi:10.1097/PAP.0b013e31823e472e

20. Lee JG, Kim S, Shim HS. Napsin A is an independent prognostic factor in surgically resected adenocarcinoma of the lung. *Lung Cancer*. 2012;77(1):156–161. doi:10.1016/j.lungcan.2012.02.013

21. Yang X, Liu Y, Lian F, et al. Lepidic and micropapillary growth pattern and expression of Napsin A can stratify patients of stage I lung adenocarcinoma into different prognostic subgroup. *Int J Clin Exp Pathol*. 2014;7(4):1459–1468.

22. Berner F, Bomze D, Lichtensteiger C, et al. Autoreactive napsin A-specific T cells are enriched in lung tumors and inflammatory lung lesions during immune checkpoint blockade. *Sci Immunol*. 2022;7(75):eabn9644–eabn. doi:10.1126/sciimmunol.abn9644

23. Uchida A, Samukawa T, Kumamoto T, et al.Napsin A levels in epithelial lining fluid as a diagnostic biomarker of primary lung adenocarcinoma. *BMC Pulm Med*. 2017;(1):17. doi:10.1186/s12890-016-0350-x

24. Li X, Lin Y, Yang Z, et al. Cancer cell membrane biomimetic nanosystem for homologous targeted dual-mode imaging and combined therapy. *J Colloid Interface Sci*. 2023;652:770–779. doi:10.1016/j.jcis.2023.08.109

25. Wang C, Wang Y, Xu L, et al. Facile aqueous-phase synthesis of biocompatible and fluorescent Ag2S nanoclusters for bioimaging: tunable photoluminescence from red to near infrared. *Small*. 2012;8(20):3137–3142. doi:10.1002/smll.201200376

26. Lababidi N, Sigal V, Koenneke A, Schwarzkopf K, Manz A, Schneider M. Microfluidics as tool to prepare size-tunable PLGA nanoparticles with high curcumin encapsulation for efficient mucus penetration. *Beilstein J Nanotechnol*. 2019;10:2280–2293. doi:10.3762/bjnano.10.220

27. Suchaoin W, de Sousa IP, Netsomboon K, Hung Thanh L, Laffleur F, Bernkop-Schnurch A. Development and in vitro evaluation of zeta potential changing self-emulsifying drug delivery systems for enhanced mucus permeation. *Int J Pharm*. 2016;510(1):255–262. doi:10.1016/j.ijpharm.2016.06.045

28. Di Giacomo C, Malfa GA, Tomasello B, Bianchi S, Acquaviva R. Natural compounds and glutathione: beyond mere antioxidants. *Antioxidants*. 2023;12(7):1445. doi:10.3390/antiox12071445

29. He H, Meng S, Li H, et al. Nanoplatform based on GSH-responsive mesoporous silica nanoparticles for cancer therapy and mitochondrial targeted imaging. *Mikrochim Acta*. 2021;188(5). doi:10.1007/s00604-021-04810-4

30. Fernandez-Ponce C, Manuel JM, Fernandez-Cisnal R, et al. Superficial characteristics and functionalization effectiveness of non-toxic glutathione-capped magnetic, fluorescent, metallic and hybrid nanoparticles for biomedical applications. *Metals*. 2021;11(3):383. doi:10.3390/met11030383

31. Gao W, Xu K, Ji L, Tang B. Effect of gold nanoparticles on glutathione depletion-induced hydrogen peroxide generation and apoptosis in HL7702 cells. *Toxicol Lett*. 2011;205(1):86–95. doi:10.1016/j.toxlet.2011.05.1018

32. Leung C, Gerard C, Gonze D. Modeling the circadian control of the cell cycle and its consequences for cancer chronotherapy. *Biology-Basel*. 2023;12(4). doi:10.3390/biology12040612

33. Matsumoto Y, Ju T. Aberrant glycosylation as immune therapeutic targets for solid tumors. *Cancers*. 2023;15(14).

34. Barabadi H, Alizadeh A, Ovais M, Ahmadi A, Shinwari ZK, Saravanan M. Efficacy of green nanoparticles against cancerous and normal cell lines: a systematic review and meta-analysis. *IET Nanobiotechnol*. 2018;12(4):377–391. doi:10.1049/iet-nbt.2017.0120

35. Ma T, Chen R, Lv N, et al. Size-transformable bicomponent peptide nanoparticles for deep tumor penetration and photo-chemo combined antitumor therapy. *Small*. 2022;18(7). doi:10.1002/smll.202106291

36. Gimondi S, de Castro JV, Reis RL, Ferreira H, Neves NM. On the size-dependent internalization of sub-hundred polymeric nanoparticles. *Colloids Surf B Biointerfaces*. 2023;225.

37. Hersh AM, Alomari S, Tyler BM. Crossing the blood-brain barrier: advances in nanoparticle technology for drug delivery in neuro-oncology. *Int J mol Sci*. 2022;23(8). doi:10.3390/ijms23084153

38. Balog S, de Almeida MS, Taladriz-Blanco P, Rothen-Rutishauser B, Petri-Fink A. Does the surface charge of the nanoparticles drive nanoparticle-cell membrane interactions? *Curr Opin Biotechnol*. 2024;87.

39. Gratton SEA, Ropp PA, Pohlhaus PD, et al. The effect of particle design on cellular internalization pathways. *Proc Natl Acad Sci USA*. 2008;105(33):11613–11618. doi:10.1073/pnas.0801763105

40. Liu X, Zhang Q, Knoll W, Liedberg B, Wang Y. Rational design of functional peptide-gold hybrid nanomaterials for molecular interactions. *Adv Mater*. 2020;32(37).

41. Wilhelm S, Tavares AJ, Dai Q, et al. Analysis of nanoparticle delivery to tumours. *Nature Rev Mater*. 2016;1(5). doi:10.1038/natrevmats.2016.14

42. Ali I, Mukhtar SD, Ai HS, Scotti MT, Scotti L. Advances in nanoparticles as anticancer drug delivery vector: need of this century. *Curr Pharm Des*. 2020;26(15):1637–1649. doi:10.2174/1381612826666200203124330

43. Baidya G, Tiwary R, Mudassir M, et al. Passive internalization and active extrusion determines PLGA-nanoparticle concentration in cancer cell lines. *Nanomedicine*. 2020;15(23):2229–2240. doi:10.2217/nnm-2020-0229

44. Cabral H, Matsumoto Y, Mizuno K, et al. Accumulation of sub-100 nm polymeric micelles in poorly permeable tumours depends on size. *Nature Nanotechnol*. 2011;6(12):815–823. doi:10.1038/nnano.2011.166

45. Sonwani S, Madaan S, Arora J, et al. Inhalation exposure to atmospheric nanoparticles and its associated impacts on human health: a review. *Front Sustain Cities*. 2021;3.

46. Mapanao AK, Giannone G, Summa M, et al. Biokinetics and clearance of inhaled gold ultrasmall-in-nano architectures. *Nanoscale Adv*. 2020;2(9):3815–3820. doi:10.1039/D0NA00521E

47. Yang L, Feuchtinger A, Moeller W, et al. Three-dimensional quantitative co-mapping of pulmonary morphology and nanoparticle distribution with cellular resolution in nondissected murine lungs. *Acs Nano*. 2019;13(2):1029–1041. doi:10.1021/acsnano.8b07524

48. Koshkina NV, Agoulnik IY, Melton SL, Densmore CL, Knight V. Biodistribution and pharmacokinetics of aerosol and intravenously administered DNA-polyethyleneimine complexes: optimization of pulmonary delivery and retention. *Mol Ther*. 2003;8(2):249–254. doi:10.1016/S1525-0016(03)00177-1

49. Jahangirian H, Kalantari K, Izadiyan Z, Rafiee-Moghaddam R, Shameli K, Webster TJ. A review of small molecules and drug delivery applications using gold and iron nanoparticles. *Int J Nanomed*. 2019;14:1633–1657. doi:10.2147/IJN.S184723

50. Yang Z, Zhao Y, Hao Y, et al. Ultrasmall red fluorescent gold nanoclusters for highly biocompatible and long-time nerve imaging. *Part Part Syst Charact*. 2021;38(5). doi:10.1002/ppsc.202100001

51. Zhang C, Wang Y, Zhao Y, et al. Biodegradable Micelles for NIR/GSH-Triggered Chemophototherapy of Cancer. *Nanomaterials*. 2019;9(1).

52. Zhao Y, Maharjan S, Sun Y, et al. Red fluorescent AuNDs with conjugation of cholera toxin subunit B (CTB) for extended-distance retro-nerve transporting and long-time neural tracing. *Acta Biomater*. 2020;102:394–402. doi:10.1016/j.actbio.2019.11.045

53. SreeHarsha N. Embelin impact on paraquat-induced lung injury through suppressing oxidative stress, inflammatory cascade, and MAPK/NF-kappa B signaling pathway. *J Biochem mol Toxicol*. 2020;34(4). doi:10.1002/jbt.22456

54. Hatware KV, Sharma S, Patil K, Shete M, Karri S, Gupta G. Evidence for gastroprotective, anti-inflammatory and antioxidant potential of methanolic extract of Cordia dichotoma leaves on indomethacin and stress induced gastric lesions in Wistar rats. *Biomed Pharmacother*. 2018;103:317–325. doi:10.1016/j.biopha.2018.04.007